Iran Agricultural Research (2025) 44 (1) 66-77.

Iran Agricultural Research

Journal homepage: https://iar.shirazu.ac.ir

Research Article

Modeling non-Newtonian liquid viscosity: Impact of temperature and concentration on the rate of occupied area variation

Seyed Mehdi Nassiri* **Ramin Rahmany** , **Mohammad Amin Nematollahi**

Department of Biosystems Engineering, School of Agriculture, Shiraz University, Shiraz, I. R. Iran

ARTICLE INFO

Keywords:
Artificial neural network
Consistency
Image processing
Mathematical modeling
Rheological properties

ABSTRACT The rheological behaviors of liquid and semi-solid foods during production processes play a critical role in the design and optimization of processing equipment. Consequently, continuous monitoring of properties such as the viscosity of non-Newtonian liquids is essential in food processing industries. To address this need, the present study explores the feasibility of using image processing techniques to estimate the apparent viscosity of non-Newtonian fluids. Both regression analysis and artificial neural network (ANN) models were developed to interpret the measured data. The regression models yielded coefficients of determination (R^2) ranging from 0.96 to 1.00, with average absolute estimation errors between 0.02% and 15.27%. Additionally, two ANN architectures, multilayer perceptron (MLP) and radial basis function (RBF), were evaluated for their predictive performance. The high correlation coefficients achieved during both training and testing phases indicate the strong predictive capability of these models. Overall, the findings support the use of image processing, specifically through analysis of surface area variations, as a viable and accurate approach for estimating the apparent viscosity of non-Newtonian liquids in food processing applications.

INTRODUCTION

The measurement of viscosity is essential at various stages of industrial food production, as it directly influences the flow behavior, appearance, and stability of liquid food products. Accurate viscosity monitoring is particularly important for controlling the quality of liquid raw materials upon entry into the production line. Pumps, which are central to the transportation of food products throughout processing and packaging stages, rely on precise viscosity data for determining power requirements and optimal pipe sizing. Thus, understanding fluid flow behavior is critical for selecting and designing suitable processing equipment. In food processing operations, viscosity can vary significantly during unit operations such as heating, cooling, concentration, and industrial fermentation. Designing efficient systems requires careful consideration of these viscosity fluctuations to ensure that equipment can accommodate the changing rheological properties of the product throughout production (Razavi, 2006). In some cases, selective or continuous (in-line) viscosity measurements are necessary to maintain product quality in real time (PCE Instruments, 2016). Traditional viscosity measurement methods typically involve direct-contact viscometers, which can be time-consuming, costly, and prone to human error. These devices may also require frequent recalibration to maintain accuracy (Bourne, 2002). A variety of viscometers have been developed to measure the viscosity of non-Newtonian fluids, including capillary tube, falling ball, cone and plate, concentric cylinder viscometers, and the Bostwick consistometer (Bhattad, 2023; Bourne, 2002). Additionally, instruments based on shear force, Stokes' law, rotational torque, and flow time have been employed to estimate apparent viscosity (Bano et al., 2003; Bhattad, 2023; Bourne, 2002; Kulicke and Clasen, 2004; Mohammadi, 2013; Noel et al., 2011; Park and Irvine, 1997; Sadat and Khan, 2007; Shin et al., 2001; Zavrsnik and Strasser, 2013). Non-invasive and real-time viscosity measurement techniques have also emerged. For instance, ultrasonic wave-based systems have been developed to monitor the viscosity of highly viscous, moving fluids without direct contact (Kazys et al., 2014). Simulations of fluid viscosity have been achieved by mapping the velocity of non-Newtonian fluids within interstitial pores (Eberhard et al., 2019; 2020). More recently, image-based methods have been introduced as a novel approach to estimate the viscosity of non-Newtonian liquids (Li et al., 2021).

The quality of semi-liquid food products has traditionally been assessed using the static surface area occupied by the liquid, as exemplified by instruments such as the Haugh meter (Bourne, 2002). However, most conventional methods and devices are designed for use in laboratory settings and lack the capability for real-time, in-line monitoring. In modern food processing industries, where product appearance and mechanical properties can vary considerably, there is a growing demand for real-time quality assessment tools. These tools must enable rapid feedback and control through programmable logic controllers (PLCs) integrated into processing lines. In this

*Corresponding Author: Associate professor, Department of Biosystems Engineering, School of Agriculture, Shiraz University, Shiraz, I. R. Iran
E-mail address: nasiri@shirazu.ac.ir
https://doi.org/10.22099/iar.2025.51629.1648
Received 08 November 2024; Received in revised form Accepted 21 February 2025; Accepted 24 February 2025
Available online 18 May 2025

context, image processing techniques have emerged as promising alternatives for estimating the apparent viscosity of non-Newtonian liquids. Nassiri et al. (2013) demonstrated that changes in the liquid's surface area over time could be used to estimate viscosity, reporting a strong linear correlation and an average relative error of 7.7%. Their findings suggest the potential for developing a simple, real-time device for viscosity measurement based on surface area variation. Similarly, Jafari and Tatar (2016) used image analysis to estimate the viscosity of date sap. By observing the shape of falling sap droplets at different temperatures and concentrations, they found the fluid's behavior followed a power-law model, confirming the effectiveness of image-based methods for characterizing non-Newtonian fluids. Other innovations in image-based viscosity estimation include measuring the dispersion of an incident light beam through a fluid in a glass cylinder (Santhosh and Shenoy, 2016), analyzing the falling velocity of a submerged ball (Tang, 2016), tracking fluid travel time between fixed points in a microchannel (Puneeth et al., 2020), and estimating shear rate in a curved capillary tube while accounting for fluid inertia (Kornaeva et al., 2023). Nevertheless, high viscosity, opacity, and the presence of solid particles in many non-Newtonian food liquids complicate the use of these methods, especially when tracking submerged objects. The novelty of the present study lies in its approach to estimating viscosity based on changes in liquid surface area—an approach that does not require object tracking within the fluid. This method offers several advantages: it supports real-time measurement, enables rapid estimation, and is cost-effective, making it a practical solution for industrial applications.

MATERIALS AND METHODS

The study was conducted in two stages. In the first stage, the apparent viscosity of a non-Newtonian fluid was measured using both a rotational viscometer and a custom image processing test rig, across varying temperatures and concentrations. In the second stage, the data collected were used to develop predictive models using regression analysis and artificial neural networks (ANN). These models were calibrated to relate the input variables, surface area, angular velocity, temperature, and concentration, to the output variable, apparent viscosity. To prepare the non-Newtonian fluid samples, Carboxymethyl Cellulose (CMC) powder (Sigma-Aldrich, 99% purity) was selected due to its stability under varying conditions and its high solubility in cold water. Different viscosity levels were achieved by dissolving varying amounts of CMC powder in distilled water. The powder was gradually added to the water while stirring, and the resulting solution was placed in an incubator shaker for 12 hours to ensure complete homogenization. To enhance contrast between the solution and the background during image analysis, 10 mL of crystal violet was added to each sample, turning the solution purple. Crystal violet was chosen since it does not affect the viscosity and is commonly used as a pH indicator. Samples were prepared at concentrations of 1.00%, 1.15%, 1.30%, 1.45%, 1.60%, and 1.75% (w/w) (Eq. (1)). Preliminary tests confirmed that even at a concentration of 1.75%, the solution exhibited high viscosity, despite the relatively low CMC content.

$$Weight\ percentage = \frac{Weight\ of\ solubel\ solid \times 100}{Weight\ of\ solvent} \quad \text{Eq. (1)}$$

A sample volume of 200 mL was used for each test, which corresponded to the minimum volume required for accurate viscosity measurement using a Brookfield rotational viscometer (Model HADVII Pro, USA). This volume ensured an appropriate clearance between the spindle and the container wall, preventing wall effects that could compromise measurement accuracy. To maintain the target temperature during measurement, the sample container was immersed in a hot water bath. Viscosity measurements were conducted using spindle number 06 at rotational speeds of 5, 10, 20, 30, 50, 60, and 100 rpm. Each measurement lasted 60 seconds, during which ten data points were recorded. The average of these ten readings was used to determine the apparent viscosity for each condition. In parallel, a custom test rig was developed to estimate viscosity using image processing techniques. The rig was designed to regulate the surrounding temperature to account for its influence on fluid viscosity (Fig. 1), ensuring consistency between measurements obtained from both the viscometer and the image processing system.

A temperature-controlled chamber with internal dimensions of $50 \times 70 \times 70$ cm^3 was constructed to facilitate consistent environmental conditions during image-based viscosity measurements. The chamber body was made of polyvinyl chloride (PVC), selected for its low thermal conductivity (0.19 W/m·K) (Onyeaju et al., 2012), which helps minimize heat loss. The top side of the chamber featured a glass door with a circular opening (6 cm in diameter), allowing for the placement of a cylindrical sample container. The temperature control system comprised a digital control unit with a display, a PT100 temperature sensor (± 0.1 °C accuracy), a 500 W heater, and a 12 V circulation fan. These components ensured stable and uniform temperature conditions inside the chamber. A schematic of the complete setup is shown in Fig. 1. A glass table was mounted within the chamber, with a high-resolution camera (XP 955M; see specifications in Table 1) fixed beneath it. The camera was oriented to capture vertical video footage of the fluid as it spread on the glass surface (Fig. 2). The camera was connected to a laptop equipped with an Intel Core i7 processor and 8 GB of RAM for data acquisition and processing. For each test, a cylindrical container filled with 200 mL of CMC solution, preconditioned to match the chamber temperature, was placed in the chamber. Upon lifting the container, the fluid spread across the glass surface. The area of the spreading liquid was measured by analyzing video frames captured at a rate of approximately eight images per second. Real-time image processing was carried out using LabVIEW 2014 software (National Instruments), which enabled the detection and quantification of surface area changes corresponding to the fluid flow behavior.

Graphical commands in the software toolkit were utilized to distinguish and separate the fluid images from the background. By adjusting the histogram in the Vision Assistant menu, the image's contrast was enhanced, making it easier to identify the fluid from its background. Subsequently, the image was converted into binary format by applying a threshold, as illustrated in Fig. 3.

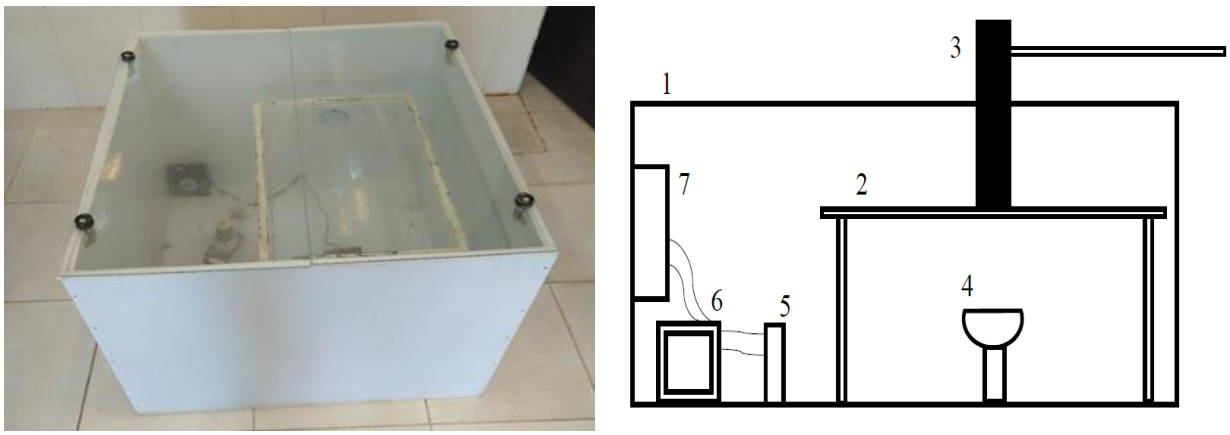

(a) (b)

Fig. 1. (a) Test rig (temperature control chamber-TCC), and (b) Schematic of TCC. 1-Main PVC chamber, 2-glass table, 3-sample container, 4- camera, 5- air circulating fan, 6- heater, and 7- temperature control unit.

Table 1. Specifications of the camera used in the research (Model 955 M)

Item	Specification
Manufacturer company	XP manufacturer, China
How to transfer	USB 2.0 data
Number of pictures per second	30 fps
Sensor type 300K Pixel CMOS Chip	640 × 480 pixels
Photo resolution quality	Up to 16 megapixels
Lens diameter	f = 3.85 mm
Automatic adjustment range	From 10 cm to infinity

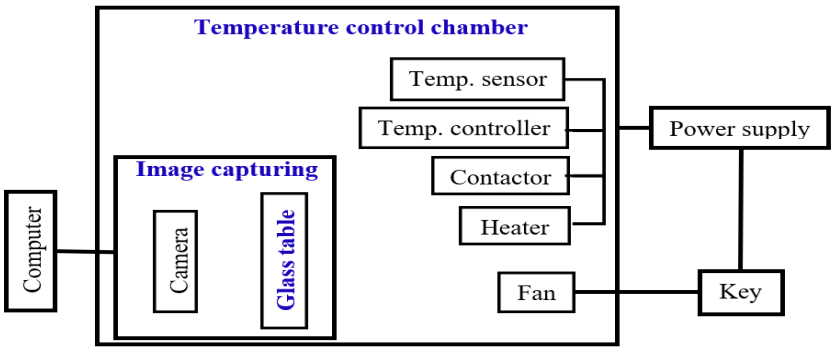

Fig. 2. Schematic of temperature control chamber.

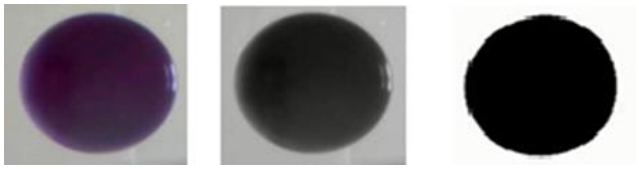

(a) (b) (c)

Fig. 3. Image segmentation and binary process. (a) original, (b) binary, and (c) eliminated background images.

The output of the image processing program was displayed as a three-column array consisting of the image capture timestamp, the number of fluid pixels detected at that time, and the corresponding surface area of the fluid. To estimate the fluid surface area, the program first identified and counted the number of pixels representing the liquid region in each image. Based on calibration, it was established that each square centimeter corresponded to an average of 454 pixels. This pixel-to-area conversion enabled accurate calculation of the fluid's surface area over time. Fig. 4 presents a flowchart detailing the image processing algorithm employed for surface area estimation.

The output data of LabVIEW were transferred to MATLAB software (version 2014) and the average velocity of fluid movement was calculated. To calculate the average rate of area change (RAC = S) of liquid, the area of liquid expansion on the glass table from zero to about a second after releasing (t_1-t_0 = 1 s) was computed by Eq. (2).

$$S = \frac{\Delta a}{\Delta s} = \frac{a_1 - a_0}{t_1 - t_0} = a_1 - a_0 \left(\mathrm{cm}^2/\mathrm{s}\right) \qquad \text{Eq. (2)}$$

where a_0 and a_1 represent the fluid surface area at the initial time and at time 1, respectively.

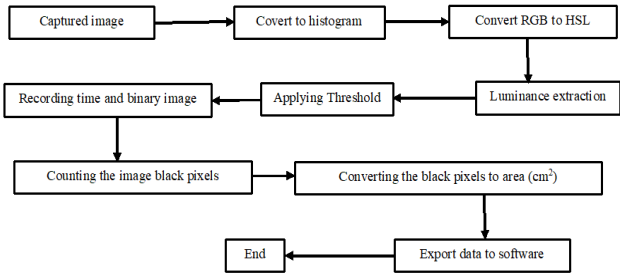

Fig. 4. Image processing flowchart.

This study aimed to investigate the influence of two key factors, solution concentration and temperature, on the average rate of change in the spreading area of the solution, with particular attention to the impact of viscosity. The solution concentration was tested at six levels: 1.00%, 1.15%, 1.3%, 1.45%, 1.6%, and 1.75% (w/w). Temperature was varied across five levels: 25, 35, 45, 55, and 65 °C (Saifur Rahman et al., 2021). Regression models were developed using SPSS (version 21, SPSS Inc.) and Minitab (version 18), with coefficients estimated via the unconstrained Levenberg–Marquardt optimization algorithm. Independent variables were selected through the "best subset" approach, guided by Mallow's C_p and the maximum adjusted coefficient of determination (Hair et al., 2009). Model performance was assessed using 10-fold cross-validation along with several statistical criteria: mean bias error (MBE), Wilmot's index of agreement (distance index) (*d*), corrected Akaike Information Criterion for small samples (AICc), Bayesian Information Criterion (BIC), and predicted residual error sum of squares (PRESS). MBE quantifies the average tendency of the predictions to under- or overestimate the observed values, while AICc and BIC provide comparative metrics for model adequacy, particularly in the presence of heteroscedasticity and differing model complexities (Brewer et al., 2016; Kuha, 2004). The formulas used to compute MBE and d are given in Eq. (3) and Eq. (4), as defined by Quej et al. (2016).

$$MBE = N^{-1}\sum_{i=1}^{N}(P_i - O_i) \qquad \text{Eq. (3)}$$

$$d = 1 - \left[\frac{\sum_{i=1}^{N}(P_i - O_i)^2}{\sum_{i=1}^{N}(|P_i - \bar{O}| + |O_i - \bar{O}|)^2}\right] \qquad \text{Eq. (4)}$$

In the above equations, P, O, and N denote the predicted value, the observed (measured) value, and the number of data points, respectively. The *d* is a metric designed to evaluate the degree of agreement between predicted and observed data series. Unlike correlation coefficients, d specifically emphasizes the accuracy of estimations rather than their linear association. It ranges from 0 to 1, with values closer to 1 indicating a stronger agreement and minimal deviation between measured and modeled results (Deo and Sahin, 2015). To enhance the reliability of the selected regression models, uncertainty analysis was conducted using the principles of uncertainty propagation. Since the models were developed based on temperature and concentration as input variables, uncertainty propagation was applied to assess the resulting uncertainty in predicted viscosity values. This approach, described by Eq. (5), allows the estimation of the combined effect of input uncertainties on the model output (Kroese et al., 2011; Skoog et al., 2007).

$$\sigma_{f(T,C)} = \sqrt{(\frac{\partial f}{\partial T})^2(\sigma_T)^2 + (\frac{\partial f}{\partial C})^2(\sigma_C)^2} \qquad \text{Eq. (5)}$$

Two classes of ANN, namely multi-layer perceptron (MLP) and radial basis function (RBF), including their structure and training process concept were assessed. The MLP and RBF are two well-known ANNs that details of their structures, training algorithms, and modeling are available in the literature (Nematollahi *et al.*, 2020; Nematollahi and Mousavi Khaneghah, 2019). A MLP is a type of well- known feed-forward ANN architecture that is shown in Fig. 5.

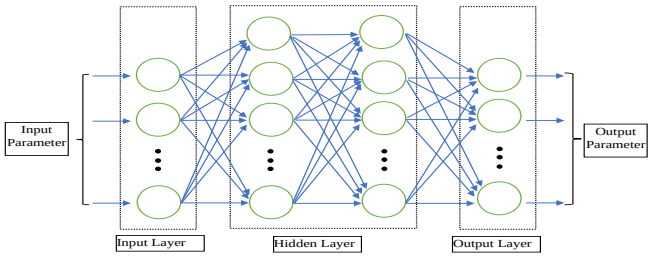

Fig. 5. Schematic representation of a multilayer perceptron ANN.

The MLP utilized the iterative back-propagation algorithm to determine the weights (W_{ij}) at each iteration (q) in the following manner [Moosavi et al., 2021; Nematollahi et al., 2020]:

$$W_{ij}(q+1) = W_{ij}(q) + \Delta W_{ij}(q) \qquad \text{Eq. (6)}$$

The generalized delta-learning rule was employed to compute the $\Delta W_{ij}(q)$ values. For example, for a single hidden layer ANN, the weights (W_{ij}) are computed as following:

$$\Delta W_{ji}(q) = \gamma f_j'(.)x_i \sum_{k=1}^{K}\{[(P_m)_k - (P_p)_k]f_k'(.)W_{kj}(q)\} + \alpha\Delta W_{ji}(q-1) \qquad \text{Eq. (7)}$$

where γ, $f'(.)$, x_i, and α are the learning rate, a derivative of the transfer (activation) function concerning its input, i^{th} input to ANN, and momentum value, respectively. Also, P_m and P_p represents target (desired) output of node k and predicted output of node k, respectively.

The RBF-ANN is a type of two-layer feed-forward ANN that is known for its fast training and widespread use, as well as its simple structure. In the RBF network, the learning process consists of two steps. The first step involves determining the parameters, such as the centers and the width of the basis functions. The second step focuses on adjusting the network weights. The RBF output is computed according to the following equation [Nematollahi and Mousavi Khaneghah, 2019]:

$$Y_k(X) = \sum_{j=1}^{n} w_{kj}\varphi_j(\|X - U_j\|) + b_k \qquad \text{Eq. (8)}$$

In the ANN models, Y_k represents the dependent variable, while X, Uj, and b_k correspond to the input vector, the vector defining the center of the basis function φ and the bias, respectively. The Gaussian function was employed as the basis function in the design of the RBF-ANN. To optimize the parameters of the MLP network, including the number of hidden layers, neurons, transfer function, and learning algorithm, multiple iterations were carried out. The primary objective was to minimize the error between the ANN's predicted output and the actual measured data. For the MLP training process, a two-hidden-layer architecture was chosen, utilizing the Levenberg-Marquardt algorithm as the learning algorithm and the sigmoid function as the transfer function. The design and training of the ANN were implemented using MATLAB software. In the RBF model, the input parameters included spindle rotational speed at seven levels (5, 10, 20, 30, 50, 60, and 100 rpm) and the RAC measured using the image processing method. The output parameter was the apparent viscosity. The network consisted of two hidden layers, with 6 neurons in the first layer and 11 neurons in the second layer. The network topology was represented as 2-6-11-1, with the logarithmic sigmoid (logsig) function as the transfer function and the Levenberg-Marquardt algorithm used for training in MATLAB. During the training and calibration process, 80% of the data was used for training, while the remaining 20% was randomly selected for testing. The performance of the trained models was evaluated using the root mean squared error (RMSE), mean absolute percentage error (MAPE), and coefficient of determination (R^2).

$$RMSE = \sqrt{\frac{\sum_{i=1}^{N}(O_i - P_i)^2}{N}} \quad \text{Eq. (9)}$$

$$MAPE = N^{-1}\sum_{i=1}^{N}\left|\frac{O_i - P_i}{O_i}\right| \times 100 \quad \text{Eq. (10)}$$

$$R^2 = 1 - [(\sum_{i=1}^{N}(P_i - O_i)^2)/(\sum_{i=1}^{N}(O_i - \bar{O})^2] \quad \text{Eq. (11)}$$

where P, O, and N refer to predicted value, observed (measured) value, and number of data points, respectively.

RESULT AND DISCUSSION

Two main factors of solution concentration and temperature, and their interaction significantly affected the rate of liquid expansion on the glass table at 1 % level of significance (Table 2). Temperature had a contrasting impact on viscosity, with concentration displaying a consistent upward influence (Fig. 6 and Fig. 7). The reduction in viscosity can be explained by the disruption of large molecular clusters. These clusters are frequently observed in polysaccharide-based polyelectrolytes when dissolved in water.

Table 2. ANOVA of RAC on glass

Source of variation	df.	MS	F
Liquid concentration	5	201916.2	1779.1**
Liquid temperature	4	93540	824.2**
Concentration × temperature	20	9801.8	86.3**
Error	120	113.4	-
Total	149	305371.4	-

** shows significant difference at 1 % probability level.

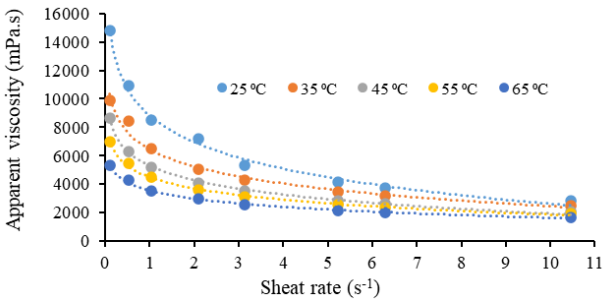

Fig. 6. Variation of apparent viscosity vs. shear rate at different temperature levels.

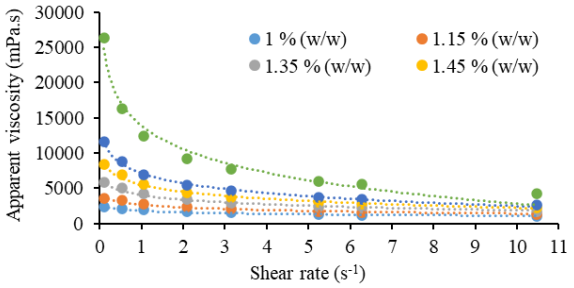

Fig. 7. Variation of apparent viscosity vs. shear rate at different concentration levels.

This implies that as temperature increases, the distance between molecules tends to expand, which reduces the solution's resistance to flow, similar to the behavior of Newtonian fluids (Abdul Wahab et al., 2019; Benchabane and Bekkour, 2008; Florence, 2023; Girado et al., 2007; Holmes et al., 2011; Yasar et al., 2007). However, in some other non-Newtonian fluids, the effect of temperature is reversed; as temperature increases, the fluid structure becomes more solid, resulting in increased resistance to flow and, consequently, higher viscosity (Bourne, 2002). In the case of most plastic fluids, apparent viscosity tends to remain more consistent at higher concentration levels, although the rate of variation decreases as the solution temperature increases. The greater differences in apparent viscosity observed at higher concentrations may be due to the particle-particle interactions (Togrul and Arsalan, 2003). Both ANOVA and graphical analysis indicate that concentration has a more significant effect on apparent viscosity variation compared to the temperature (Fig. 8), which aligns with the findings of Kulicke and Clasen (2004). Apparent viscosity followed a logarithmic trend with respect to shear rate, indicating a plastic behavior for the CMC solution. This observation is consistent with the findings of Yaseen et al. (2005). CMC solutions with concentrations ranging from 0.2% to 7% (w/w) exhibited behavior consistent with the Cross (a type of power) model at 20 °C (Benchabane and Bekkour, 2008). Togrul et al. (2003) found that CMC solutions with a degree of substitution (DS) of 0.667 exhibited pseudoplastic behavior, which they described using a power law relationship.

The expansion area of the solution on the glass was influenced by the temperature and concentration of the fluid (Fig. 9 and Fig. 10). The RAC increased rapidly within one second of solution release and then leveled off, indicating two distinct regimes in the graphs.

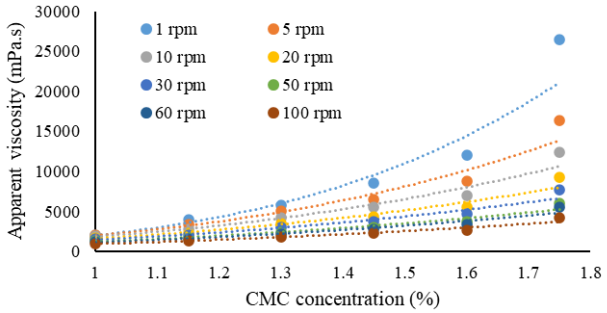

Fig. 8. Variation of apparent viscosity vs. concentration levels at different spindel rotational speeds (shear rate).

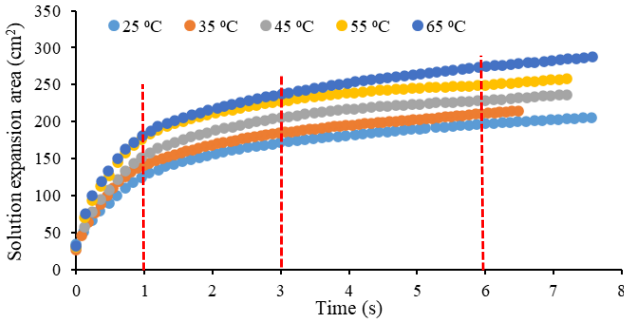

Fig. 9. Solution expansion area at different temperatures for 1.3% concentration.

A transition point in the area change trend was observed at approximately one second for both concentration and temperature-based graphs. When the trends were plotted on a semi-logarithmic scale, the different regimes became more distinct, as shown in Fig. 11. As a result, three distinct zones were identified for model development. The first zone extended from the start to about one second, the second zone spanned approximately one to two seconds, and the third zone ranged from three to six seconds, where the rate of area change followed a nearly linear trend, as illustrated in Fig. 11. Thus, Eq. (2) was used to calculate the RAC for all zones at different levels of solution concentration and temperature. It was observed that the RAC values between one to two seconds and three to six seconds showed weak correlations with the measured viscosity and were not suitable parameters for model development. This can be attributed to the slopes of the curves in these two linear intervals, as demonstrated in Fig. 11.

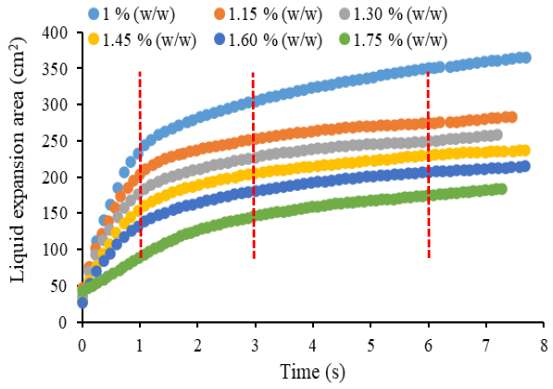

Fig. 10. Liquid expansion area of different concentration levels at 55 ºC.

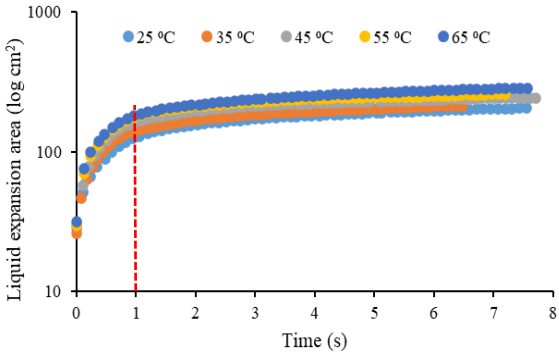

Fig. 11. Log liquid expansion area at different temperatures for 1.3 % concentration.

As a result, next attempt was made based on the slope of the curves between zero and one second after the movement of the solution, during which all curves almost exhibited a nonlinear trend. As shown in Fig. 11, the RAC varied significantly at different temperature levels (25 to 65 ºC). The same was followed at different solution concentrations. Initially, the correlation between each pair of RAC and concentration, as well as RAC and temperature, was visualized using scatter plots. It was observed that the RAC followed a nonlinear relationship with concentration (C) and temperature (T). Therefore, different relationships between RAC and C, T, T^2, and C^2 were evaluated using the best subset regression modeling method (Kulicke and Clasen, 2004). According to the Mallow's index (C_p), the following relationship was selected as the best fit (Hair et al., 2009).

$$RAC = S = 349.1C + 2.05T - 211.6C^2 \ (\text{cm}^2/\text{s}) \quad \text{Eq. (12)}$$
$$(34.82^{***}) \ (18.67^{***}) \ (-39.93^{***})$$

Second row figures (in Eq. (12)) show the amount of "t" value of regression coefficients and exponent stars refer to significance (probability) level of "t" values. It is clear that all coefficients are significant at 1 % level of probability. Overall, F value shows that the regression model could significantly explain variation of RAC based on change in temperature and concentration (Table 3) and in good condition for generalization. The summary of the model is given in Table 4. 10-fold R^2 as a model validation index, emphasizes on the strength of regression model for generalization.

Table 3. ANOVA for regression model (Eq. (12))

Source	df	SS	MS	F-Value	P-Value
Regression	3	4438210	1479403	4058.48	0.000
Error	147	53585	365		
Total	150	4491795			

Table 4. Model summary of regression model (Eq. (12)) statistical indices

C_p	R^2	10-fold R^2	Predict R^2	SEE	10-fold SEE	Lack-of-Fit
3	0.988	0.987	0.988	19.09	19.59	0.000

As the primary goal was to assess the feasibility of determining the RAC of a non-Newtonian fluid, the RAC at various treatments was correlated with the corresponding measured apparent viscosity of the samples. A nonlinear relationship was observed between RAC and apparent viscosity. According to the trend of scatter data plots, two types of relationships were established and evaluated (Eq. (13) and Eq. (14)).

$$V = e^{a-b(S)} \quad \text{Eq. (13)}$$

$$V = a - bln(\ln(S)) \quad \text{Eq. (14)}$$

The *a* and *b* are equation constants and *S* is RAC. Each model was established by converting the x or y axis to natural log format. All relationship coefficients were computed at different spindle rotational speed (shear rate) and reported in Table 5 and Table 6.

According to the table, the model based on viscosity data transformation (Ln transformation) has followed closer to the measured value as compared to RAC data transformation (Ln transformation). However, the AICc values revealed that model at spindle rotational speed of 100 rpm (10.47 s^{-1} shear rate) was the best one amongst the models for both kinds of data set transformations. The final selected model for prediction of viscosity as a function of RAC is proposed in Eq. (15).

$$V = e^{8.71-0.007(S)} = 6063e^{-0.007(S)} \quad \text{Eq. (15)}$$

The normal probability plot and residual versus fitted values plot indicate that the modeling assumptions of normality and homoscedasticity of residuals were within acceptable limits (Fig. 12).

Table 5. Model coefficients (a and b) and statistical indices for Eq. (13)

rpm	Shear rate (s^{-1})	$V = e^{a-b(S)}$									
		a	b	R^2	SEE	F	10-f R^2	10-f SEE	AICc	BIC	PRESS
5	0.52	10.20	0.01	90.2	0.24	257.6***	88.6	0.25	4.46	7.74	1.87
10	1.05	9.87	0.009	91.6	0.20	306.8***	90.4	0.21	-5.93	-2.65	1.23
20	2.09	9.54	0.008	92.0	0.18	320.4***	90.8	0.19	-12.98	-9.70	1.04
30	3.14	9.33	0.008	92.1	0.17	327.8***	91.0	0.17	-16.77	-13.49	0.92
50	5.23	9.10	0.008	93.0	0.15	373.0***	92.1	0.16	-22.98	-19.70	0.74
60	6.28	9.0	0.008	91.4	0.15	396.4***	92.53	0.15	-24.88	-21.60	0.69
100	**10.47**	**8.71**	**0.007**	**93.6**	**0.14**	**410.5*** **	**92.9**	**0.14**	**-29.20**	**-25.92**	**0.60**

*** shows significant difference at 1% level of probability, SEE,10-f, AICc and BIC are standard error of estimate, 10-fold, corrected Akaike information criterion and Bayesian information criterion, respectively.

Table 6. Model coefficients (a and b) and statistical indices for Eq. (14)

rpm	Shear rate (s^{-1})	$V = a - bln(\ln(S))$									
		a	b	R^2	SEE	F	10-f R^2	10-f SEE	AICc	BIC	PRESS
5	0.52	68168	38534	89.2	1862	384.1***	86.8	1987	525.8	531.1	7.42×10^7
10	1.05	50479	28277	89	1378	227.4***	87	1447	523.7	527.0	6.31×10^7
20	2.09	36194	20040	89.4	957	237.1***	87.8	994	501.8	505.1	2.98×10^7
30	3.14	29513	16242	90.8	749	254.4***	88.6	775	487.1	490.4	1.82×10^7
50	5.23	22799	12470	91	546	281.5***	89.6	567	468.2	471.5	9.73×10^6
60	6.28	20702	11300	91.1	489	288.1***	89.7	511	461.6	464.9	7.91×10^6
100	**10.47**	**15459**	**8364**	**91**	**365**	**284.5*** **	**89.3**	**385**	**443.9**	**447.2**	**4.52×10^6**

*** shows significant difference at 1% level of probability, SEE,10-f, AICc and BIC are standard error of estimate, 10-fold, corrected Akaike information criterion and Bayesian information criterion, respectively.

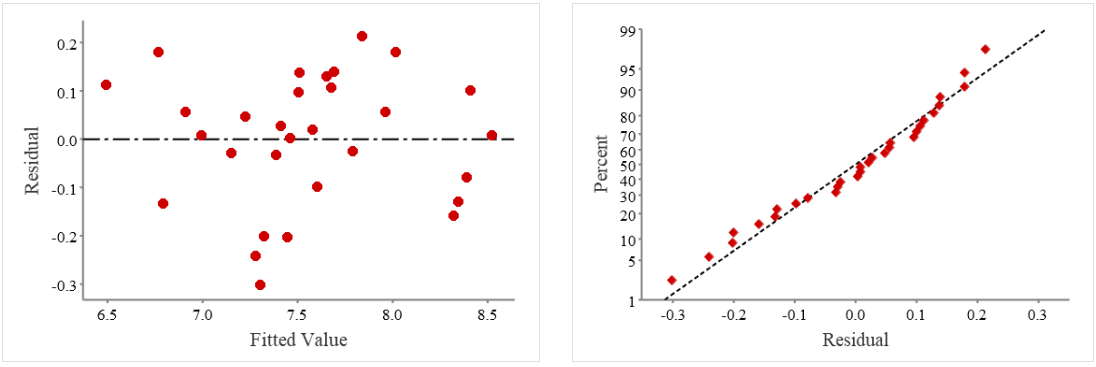

(a) (b)

Fig. 12. (a) Residual vs. fitted values and (b) normal probability plot of residuals.

By substituting the Eq. (12) into Eq. (15), Eq. (16) was derived that establishes a correlation between temperature, concentration, and viscosity (Kulicke and Clasen, 2004). When applying the model to the measured values of temperature and concentration within the experimental range, the calculated MBE and *d* were found to be 48.18 mPa.s and 0.991, respectively at 100 rpm (10.47 s^{-1}). These results indicate that the model accurately and precisely estimated the viscosity of the non-Newtonian solution, with only a negligible overestimation (Fig. 13). At higher rotational speeds, discriminant differences were observed amongst the viscosity of samples at different concentrations and temperature levels. Therefore, more precise model training occurred at the higher shear rates of spindle, especially at 100 rpm.

$$V = f(C,T) = 6063e^{(211.6C^2 - 349.1C - 2.05T)} \quad \text{Eq. (16)}$$

By taking into account the mathematical principles of uncertainty propagation, the modeled RAC of the fluid (Eq. (12)), uncertainty of RAC can be simplified as Eq. (17).

$$\sigma_S = \sqrt{(4.2\sigma_T^2) + [\sigma_C^2(349.1 - 423.3C)^2]} \ (\frac{cm^2}{s}) \quad \text{Eq. (17)}$$

As is obvious from Eq. (17), the uncertainty of RAC is affected by the uncertainty of the temperature and uncertainty of concentration as well as the amount of concentration. The same manner was followed for computing the uncertainty of the modeled viscosity by considering Eq. 13, and the uncertainty of RAC (σ_S). Finally, the total uncertainty of the viscosity can be described by Eq. (18) (Skoog et al., 2007).

$$\sigma_v = a\sigma_S e^{-b(S)}_{(\text{mPa.s})} \quad \text{Eq. (18)}$$

The values of *a* and *b* is listed in Table 7 at different rotational speeds (shear rate) of spindle. Since modeled viscosity would be matched with the corresponding values measured from viscometer outputs at the same condition, and taking into account the outputs of the Table 5 and Table 6 for selection of the best model for viscosity prediction (at rpm = 100), and assumption of 1 ºC and 0.1 % uncertainty for temperature and concentration, respectively, total uncertainty of the model is summarized in Table 8. The relative uncertainty is limited to approximately ± 0.04 or 4% at lower solution concentration.

As previously mentioned, the identical dataset for the interval of zero to one second underwent analysis using MLP and RBF ANNs. In order to predict the apparent viscosity, input parameters considered were temperature at five levels (25, 35, 45, 55, and 65 °C) and concentration at six levels (1.15%, 1.3%, 1.45%, 1.6%, and 1.75%). The performance metrics of MLP and RBF models for prediction of RAC as function of temperature and concentration were measured and compared to the corresponding relation modeled by regression (Eq. (12)). Metrics are listed in Table 9.

Based on the statistical metrics presented in Table 10, it is evident that the viscosity values obtained from the viscometer at higher rotational speeds exhibited a closer agreement with the modeled viscosity for both the ANN and MLR models. Furthermore, the results obtained from the ANN models validated the outcomes of the MLR predictions.

However, a closer examination of MBE and Willmott distance (d) showed that both the ANN models possess the capability to predict viscosity based on the rate of area change within the time frame of zero to one second after the release of the solution. These metrics were computed 0.1 mPa.s and 1, respectively for RBF model and correspondingly 1.2 mPa.s and 1 for MLP model at 100 rpm. The values are graphically demonstrated in Fig. 14 and can be compared to Fig. 13 for MLR with the same metrics with the values of 48.18 mPa.s and 0.991, respectively at 100 rpm (10.47 s^{-1}).

It is implied from the results that if an image-gathering and processing hardware is installed on a processing line of a non-Newtonian fluid, it is more accurate to develop ANN models for viscosity estimation. However, multiple linear regression gives a visual equation in hand to use at any moment to estimate the apparent viscosity with acceptable accuracy.

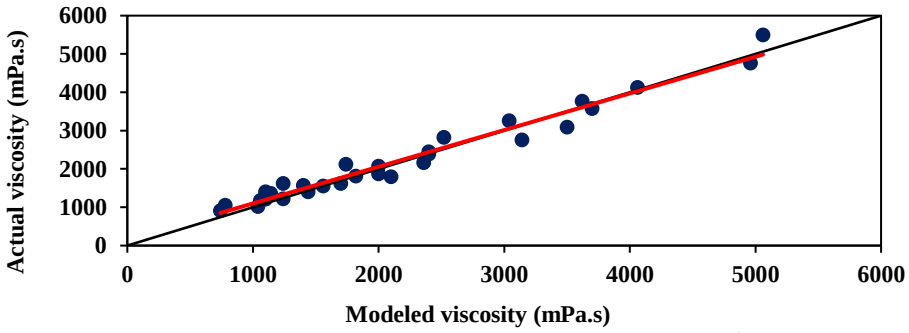

Fig. 13. Modeled vs. actual viscosity to visualize model accuracy at 100 rpm (10.47 s^{-1} shear rate).

Table 7. Eq. (18) constants of *a* and *b*

Spindle rpm	Shear rate (s^{-1})	a	b
5	0.52	269.0	0.01
10	1.05	174.0	0.009
20	2.09	111.2	0.008
30	3.14	90.2	0.008
50	5.23	71.6	0.008
60	6.28	64.8	0.008
100	**10.47**	**42.4**	**0.007**

CONCLUSION

The study hypothesized that the area occupied by a non-Newtonian liquid during free flow can estimate its apparent viscosity. Since real-time measurement of non-Newtonian food liquid viscosity is crucial during processing, the rate of area expansion (rate of change) was analyzed using image processing, and the results were modeled with multiple regression and ANNs. An exponential relationship was established for estimating apparent viscosity based on the computed rate of change in liquid expansion area (RAC = S), represented as $V = ae^{-b(S)}$ through multiple regression analysis. However, the RBF-ANN model provided more accurate results. Additionally, the study aimed to create a general model that accounted for temperature and concentration effects on viscosity. Both parameters were incorporated into the regression and ANN models, which were calibrated accordingly. The findings confirm that both models effectively estimated the viscosity of the non-Newtonian liquid (CMC solution). Future efforts could focus on developing a user-friendly device that leverages these concepts, incorporating more parameters for verification, while ensuring rapid results for real-time monitoring in a portable format.

Table 8. RAC, viscosity, and relative uncertainties at different solution concentration levels for spindle rpm = 100 (10.47 s^{-1})

Concentration (%)	σ_S (cm^2/s)	$Viscosity_{mean}$ (mPa.s)	Viscosity uncertainty (mPa.s)	$Relative\ uncertainty_{mean}$ (SE/V)
1	2.078*	1211.80	46.07	0.04
1.15	2.078	1356.39	45.90	0.03
1.3	2.078	1624.42	45.73	0.03
1.45	2.078	2081.49	45.56	0.02
1.6	2.078	2853.72	45.40	0.02
1.75	2.078	4186.09	45.23	0.01

RAC, SE and V are rate of area change, standard error and viscosity, respectively. * Difference is at the four decimal digit.

Table 9. Modeling statistics of ANN (MLP and RBF) and MLR for RAC as function of concentration and temperature

Model	d	MAPE (%)	RMSE (cm^2/s)	R^2
MLP	0.999	2.29	4.87	0.995
RBF	0.999	2.18	4.59	0.996
MLR	0.982	14.92	18.16	0.932

ANN (artificial neural network), MLP (multi-layer perceptron), RBF (radial basis function), MLR (multiple linear regression), RAC (rate of area change), MAPE (mean absolute of percentage error), RMSE (root of mean square of errors)

Table 10. Modeling statistics of ANN (MLP and RBF) and MLR for viscosity prediction

ANN (artificial neural network), MLP (multi-layer perceptron), RBF (radial basis function), MLR (multiple linear regression),

Model	rpm	Based on measured RAC				Based on modelled RAC			
		d	MAPE (%)	RMSE (cm^2/s)	R^2	d	MAPE (%)	RMSE (cm^2/s)	R^2
MLP	5	0.999	3.05	233.9	0.998	0.995	10.82	753.1	0.979
	10	0.999	2.34	205.6	0.998	0.993	9.93	692.9	0.973
	20	0.999	2.90	153.9	0.997	0.993	9.06	491.9	0.973
	30	0.999	2.58	131.5	0.997	0.993	8.46	400.3	0.972
	50	0.999	2.58	112.2	0.996	0.992	7.78	308.1	0.968
	60	0.999	2.52	100.7	0.996	0.993	7.73	274.6	0.972
	100	**1.000**	**0.19**	**15.9**	**0.999**	**0.994**	**6.24**	**185.6**	**0.975**
RBF	5	1	0.09	16.5	1	1	0.38	75.84	0.999
	10	1	0.09	8.8	1	1	0.32	53.23	0.999
	20	1	0.03	3.7	1	1	0.30	43.97	0.999
	30	1	0.06	3.7	1	1	0.27	33.30	0.999
	50	1	0.02	2.3	1	1	0.25	24.73	0.999
	60	1	0.02	1.8	1	1	0.24	22.62	0.999
	100	**1**	**0.02**	**1.8**	**1**	**1**	**0.23**	**19.65**	**0.999**
MLR	5	0.992	15.27	928.9	0.971	0.967	20.48	1899.1	0.880
	10	0.992	13.99	715.7	0.968	0.968	17.09	1369.6	0.884
	20	0.994	13.14	488.4	0.971	0.971	15.67	922.6	0.895
	30	0.993	10.17	376.8	0.973	0.974	13.65	704.9	0.906
	50	0.992	9.14	302.0	0.971	0.977	12.91	513.6	0.914
	60	0.990	9.93	308.7	0.962	0.978	12.63	445.1	0.921
	100	**0.991**	**10.08**	**221.4**	**0.965**	**0.983**	**11.66**	**296.8**	**0.936**

RAC (rate of area change), MAPE (mean absolute of percentage error), RMSE (root of mean square of errors), d (distance index)

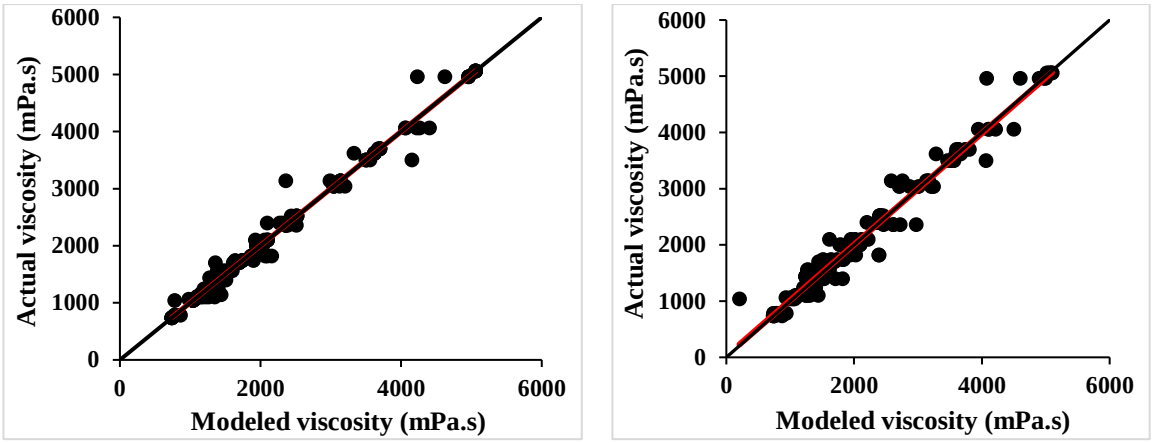

Fig. 14. Modeld vs. actual viscosity to visulize model accuracy at 100 rpm (10.47 s^{-1} shear rate). (a) RBF model and (b) MLP model.

FUNDING

This work was supported by Shiraz University Grant number 1971.

CRediT AUTHORSHIP CONTRIBUTION STATEMENT

Conceptualization: Seyed Mehdi Nassiri; Methodology: Seyed Mehdi Nassiri; Supervision: Seyed Mehdi Nassiri; Funding acquisition: Seyed Mehdi Nassiri; Project administration: Seyed Mehdi Nassiri; Resources: Seyed Mehdi Nassiri; Software: Ramin Rahmany; Investigation: Ramin Rahmany; Data curation: Ramin Rahmany; Analysis: Ramin Rahmany; Original draft preparation: Ramin Rahmany; Modelling: Seyed Mehdi Nassiri and Mohammad Amin Nematollahi; Review: Seyed Mehdi Nassiri and Mohammad Amin Nematollahi; Final corrections: Seyed Mehdi Nassiri and Mohammad Amin Nematollahi.

DECLARATION OF COMPETING INTEREST

There is no conflict of interest among the authors regard to this research.

DATA AVAILABILITY

The data that support the findings of this study are available from the corresponding author upon reasonable request.

ETHICAL STATEMENT

This research complied with ethical principles in data collection, analysis, and reporting. The authors adhered to all relevant guidelines regarding data protection, plagiarism, and responsible authorship. No human or animal subjects were involved.

ACKNOWLEDGMENTS

This research was supported by Shiraz University's Vice-Presidency Department for Research and Technology, for which we are grateful.

REFERENCES

Abdul Wahab, H., Zeb, H., Bhatti, S., Gulistan, M., Kadry, S., & Nam, Y. (2019). Numerical study for the effects of temperature dependent viscosity flow of non-Newtonian fluid with double stratification. *Applied Science*, *10*, 708. https://doi.org/10.3390/app10020708

Bánó, M., Strharsky, I., & Hrmo, I. (2003). A viscosity and density meter with a magnetically suspended rotor. *Review of Scientific Instruments*, *74*(11), 4788-4793. https://doi.org/10.1063/1.1614881

Benchabane, A., & Bekkour, K. (2008) Rheological properties of carboxymethyl cellulose (CMC) solutions. *Colloid Polymer Science*, *286*, 1173-1180. https://doi.org/10.1007/s00396-008-1882-2

Bhattad, A. (2023). Review on viscosity measurement: devices, methods and models. *Journal of Thermal Analysis and Calorimetry*, *148*, 6527-6543. https://doi.org/10.1007/s10973-023-12214-0

Bourne, M. C. (2002). *Food texture and viscosity: Concept and measurement*. New York: Academic Press.

Brewer, M. J., Butler, A., & Cooksleym, S. L. (2016) The relative performance of AIC, AICC and BIC in the presence of unobserved heterogeneity. *Methods in Ecology and Evolution*, *16*(7), 679-692. https://doi.org/10.1111/2041-210X.12541

Deo, R. C., & Şahin, M. (2015). Application of the extreme learning machine algorithm for the prediction of monthly effective drought index in eastern Australia. *Atmospheric Research*, *153*, 512-525. https://doi.org/10.1016/j.atmosres.2014.10.016

Eberhard, U., Seybold, H. J., Floriancic, M. G., Bertsch, P., Jimenez-Martinez, J., Andrade, J. S., & Holzner, M. (2019). Determination of the effective

viscosity of non-Newtonian fluids flowing through porous media. *Frontiers in Physics*, 7, 71. https://doi.org/10.3389/fphy.2019.00071

Eberhard, U., Seybold, H. J., Secchi, E., Jimenez-Martinez, J., Ruhs, P. A., Ofner, A., Andrade Jr., J. S., & Holzner, M. (2020). Mapping the local viscosity of non-Newtonian fluids flowing through disordered porous structures. *Scientific Reports, 10*, 11733. https://doi.org/10.1038/s41598-020-68545-7

Florence, A., D. (2023). Temperature-dependent variable viscosity and thermal conductivity effects on non-Newtonian fluids flow in a porous medium. *World Journal of Engineering*, *20*(3), 445-457. https://doi.org/10.1108/WJE-03-2021-0130

Girado, S., Cingolani, R., & Pisignano, D. (2007). Investigating the temperature dependence of the viscosity of a non-Newtonian fluid within lithographically defined microchannels. *The Journal of Chemical Physics,127*, 164701. https://doi.org/10.1063/1.2789426

Hair, Jr. J. F., Black, W. C., Babin, B. J., & Anderson, R. E. (2009). *Multivariate data analysis*. New Delhi: Pearson Publication.

Holmes, M. J., Parker, N. G., & Povey, M. J. W. (2011) Temperature dependence of bulk viscosity in water using acoustic spectroscopy. *Journal of Physics: Conference Series, 269*, 012011. https://doi.org/10.1088/1742-6596/269/1/012011

Jafari, A. A., & Tatar, A. (2016). Using image processing technique fin determining liquid viscosity (Case study: Date syrup). Presented at the 10Th National Conference on Iran Agricultural Machinery (Biosystems) and Mechanization, Mashhad: Ferdowsi University of Mashhad. (In Persian)

Kazys, R., Mazeika, L., Sliteris, R., & Raisutis, R. (2014) Measurement of viscosity of highly viscous non-Newtonian fluids by means of ultrasonic guided waves. *Ultrasonics*, *54*, 1104-1112. https://doi.org/10.1016/j.ultras.2014.01.007

Kroese, D. P., Taimre, T., & Botev, Z. I. (2011). *Handbook of Monte Carlo methods*. New York: John Wiley & Sons.

Kornaeva, E. P., Stebakov, I. N., Koenaev, A. V., Dremin, V. V., Popov, S. G., & Vinokurov, A. Y. (2023). A method to measure non-Newtonian fluid viscosity using inertial viscometer with a computer vision system. *International Journal of Mechanical Sciences, 242*, 107967. https://doi.org/10.1016/j.ijmecsci.2022.107967

Kuha, J. (2004) AIC and BIC: Comparisons of assumptions and performance. *Sociological Methods & Research*, *33*(2), 188-229. https://doi.org/10.1177/0049124103262065

Kulicke, W. M., & Clasen, C. (2004) *Viscosimetry of polymers and polyelectrolytes*. Berlin: Springer Berlin Heidelberg.

Li, H., Flé, G., Bhatt, M., Qu, Z., Ghazavi, S., Yazdani, L., Bosio, G., Rafati, I., & Cloutier, G. (2021). Viscoelasticity imaging of biological tissues and single cells using shear wave propagation. *Frontier Physics*, *9*, 666192. https://doi.org/10.3389/fphy.2021.666192

Mohammadi, S. M. (2013) Design and development of a viscosity and molecular weight measurement device of food fluids with variable temperature and evaluation of its performance. Proceeding of 7th national student conference of Mechanical Engineering, Karaj. Karaj: Tehran University. (In Persian)

Moosavi, A. A., Nematollahi, M. A., & Rahimi, M. (2021). Predicting water sorptivity coefficient in calcareous soils using a wavelet–neural network hybrid modeling approach. *Environmental Earth Sciences*, *80*(6), 226. https://doi.org/10.1007/s12665-021-09518-5

Munigela, N., Puranam, S. A., Goel, S., & Puneeth, S. B., (2020). Automated mini-platform with 3-D printed paper microstrips for image processing-based viscosity measurement of biological samples. IEEE Transactions on Electron Devices, 67(6), 2559-2565. https://doi.org/10.1109/TED.2020.2989727

Nassiri, S. M., Bakhshipour, A., Heydari Foroshani, M. M., & Barzegar Marvasti, M. (2013). Estimation of apparent viscosity of non-Newtonian fluids using image processing. Presented at the 8th National Conference on Iran Agricultural Machinery (Biosystems) and Mechanization, Mashhad: Ferdowsi University of Mashhad. (In Persian)

Nematollahi, M. A., Jamali, B., & Hosseini, M. (2020). Fluid velocity and mass ratio identification of piezoelectric nanotube conveying fluid using inverse analysis. *Acta Mechanica*, *231*(2), 683-700. https://doi.org/10.1007/s00707-019-02554-0

Nematollahi, M. A., & Mousavi Khaneghah, A. (2019). Neural network prediction of friction coefficients of rosemary leaves. *Journal of Food Process Engineering*, *42*(6), e13211. https://doi.org/10.1111/jfpe.13211

Noël, M., Semin, B., Hulin, J., & Auradou, H. (2011). Viscometer using drag force measurements. *Review of Scientific Instruments*, *82*(2), 109. https://doi.org/10.1063/1.3556445

Onyeaju, M. C., Osarolube, E., Chukwuocha, E. O., Ekuma, C. E., & Omasheye, G. A. J. (2012). Comparison of the thermal properties of asbestos and polyvinylchloride (PVC) ceiling sheets. *Material Science and Applied*, *3*, 240-244. https://doi.org/10.4236/msa.2012.34035

Park, N. A., & Irvine Jr, T. F. (1997). Liquid density measurements using the falling needle viscometer. *International Communications in Heat and Mass Transfer*, *24*(3), 303-312. https://doi.org/10.1016/S0735-1933(97)00016-X

PCE Instruments. (2016). The importance of viscosity measurement in food production and processing. Retrieved from: https://www.newfoodmagazine.com/news/23734/importance-viscosity-measurement-food-production-processing.

Quej, V. H., Almorox, J., Ibrakhimov, M., & Saito, L. (2016) Empirical models for estimating daily global solar radiation in Yucatán Peninsula, Mexico. *Energy Conversion and Management*, *110*, 448-456. https://doi.org/10.1016/j.enconman.2015.12.050

Razavi, M. A. (2006) *Biophysical properties of agricultural products and food materials*. Mashhad. Mashhad: Ferdowsi University of Mashhad Press. (In Persian)

Sadat, A., & Khan, I. A. (2007) A novel technique for the measurement of liquid viscosity. *Journal of Food Engineering*, *80*(4), 1194 -1198. https://doi.org/10.1016/j.jfoodeng.2006.09.009

Saifur Rahman, M., Saif Hasan, M., Nitai, A. S., Nam, S., Karmakar, A. K., Shsan, M. S., Shiddiy, M. J. A., & Ahmed, M. B. (2021) Recent developments of Carboxymethyl cellulose. *Polymers*, *13*, 1345. https://doi.org/10.3390/polym13081345

Santhosh, K. V., & Shenoy, V. (2016) Analysis of liquid viscosity by image processing technique. *Indian Journal of Science and Technology*, *9*(30), 1-7. 10.17485/ijst/2016/v9i30/98693

Shin, S., Lee, S. W., & Keum, D. Y. (2001) A new mass-detecting capillary viscometer. *Review of Scientific Instruments*, *72*(7), 3127-3128. https://doi.org/10.1063/1.1378339

Skoog, D., Holler, J., & Crouch, S. (2007). *Principles of instrumental analysis*. (6th Ed). Belmont: Thomson Brooks/Cole publisher.

Tang, J. X. (2016). Measurements of fluid viscosity using a miniature ball drop device. *Review of Scientific Instruments*, *87*(5), 054301. https://doi.org/10.1063/1.4948314

Togrul, H., & Arsalan, N. (2003). Production of carboxymethyl cellulose from sugar beet pulp cellulose and rheological behaviour of carboxymethyl cellulose. *Carbohydrate Polymers*, *45*, 73-82. https://doi.org/10.1016/S0144-8617(03)00147-4

Yasar, F., Togrul, H., & Arslan, N. (2007). Flow properties of cellulose and carboxymethyl cellulose from orange peel. *Journal of Food Engineering*, *81*, 187-199. https://doi.org/10.1016/j.jfoodeng.2006.10.022

Yaseen, E. I., Herald, T. J., Aramouni, F. M., & Alavi, S. (2005) Rheological properties of selected gum solutions. *Food Research International*, *38*, 111-119. https://doi.org/10.1016/j.foodres.2004.01.013

Zavrsnik, M., & Strasser, M. J. (2013). Line viscometry for non-Newtonian viscosity characterization. *Sensors*, 587-591. https://doi.org/10.5162/sensor2013/D7.2

Nomenclatures

Abbreviations		**Symbols and Greek letters**			
CMC	Carboxymethyl Cellulose	C_p	Mallow's index	P_m	Target output of node k
RAC=S	Rate of area change	d	Wilmot distance index	P_p	Predicted output of node k
MBE	Mean bias error	σ	Uncertainty	k	No. of ANN neurons
AIC	Akaike Information Criterion	T	Temperature	Y_k	Dependent variable
BIC	Bayesian Information Criterion	C	Concentration	φ_J	Basis function
PRESS	Prediction Residual Error Sum of Squares	$f`(.)$	Derivative of transfer function	U_j	Center of basis function vector
ANN	Artificial neural network	∂f/∂T	Partial derivative	X	Input matrix
MLP	Multi-layer perceptron	W_{ij}	ANN weights	b_k	Bias at node k
RBF	Radial basis function	q	Calculation iteration	R^2	Coefficient of determination
RMSE	Root mean squared error	γ	Learning rate	V	Apparent viscosity
MAPE	Mean absolute percentage error	x_i	i^{th} input in ANN		
MLR	Multiple linear regression	α	Momentum value		